*remote sensing*

MDPI

*Article*

# Surface Profile Recovery from Electromagnetic Fields with Physics-Informed Neural Networks

**Yuxuan Chen [1,*,†], Ce Wang [2,†], Yuan Hui [3,†], Nirav Vasant Shah [4] and Mark Spivack [5]**

[1] School of Mathematical Sciences, Soochow University, Suzhou 215006, China
[2] School of Science, Sun Yat-sen University, Shenzhen 518107, China; wangc79@mail.sysu.edu.cn
[3] Shaanxi Logistics Group Co., Ltd., Xi'an 710075, China; huiyuan.ict@gmail.com
[4] Department of Engineering, University of Cambridge, Cambridge CB2 1PZ, UK; nvs31@cam.ac.uk
[5] Department of Applied Mathematics and Theoretical Physics, University of Cambridge, Cambridge CB3 0WA, UK; ms100@cam.ac.uk
* Correspondence: chenyx@suda.edu.cn
† These authors contributed equally to this work.

**Abstract:** Physics-informed neural networks (PINN) have shown their potential in solving both direct and inverse problems of partial differential equations. In this paper, we introduce a PINN-based deep learning approach to reconstruct one-dimensional rough surfaces from field data illuminated by an electromagnetic incident wave. In the proposed algorithm, the rough surface is approximated by a neural network, with which the spatial derivatives of surface function can be obtained via automatic differentiation, and then the scattered field can be calculated using the method of moments. The neural network is trained by minimizing the loss between the calculated and the observed field data. Furthermore, the proposed method is an unsupervised approach, independent of any surface data, where only the field data are used. Both transverse electric (TE) field (Dirichlet boundary condition) and transverse magnetic (TM) field (Neumann boundary condition) are considered. Two types of field data are used here: full-scattered field data and phaseless total field data. The performance of the method is verified by testing with Gaussian-correlated random rough surfaces. Numerical results demonstrate that the PINN-based method can recover rough surfaces with great accuracy and is robust with respect to a wide range of problem regimes.

**Keywords:** deep learning; physics-informed neural network; inverse electromagnetic scattering; method of moments; rough surface reconstruction



**Citation:** Chen, Y.; Wang, C.; Hui, Y.; Shah, N.V.; Spivack, M. Surface Profile Recovery from Electromagnetic Fields with Physics-Informed Neural Networks. *Remote Sens.* **2024**, *16*, 4124. https://doi.org/10.3390/rs16224124

Academic Editor: Davide Comite

Received: 22 October 2024
Revised: 30 October 2024
Accepted: 30 October 2024
Published: 5 November 2024



## 1. Introduction

Wave propagation from rough surfaces is of crucial importance in the field of electromagnetic scattering and has been extensively studied. The inverse problem of rough surface profile recovery from scattered electromagnetic fields remains a challenging and unresolved issue. This problem is vital in remote sensing and geophysics, where accurate ground surface reconstructions are essential for applications such as radar-based soil moisture estimation, subsurface mineral detection, and the assessment of glacier and ice sheet dynamics. Precise surface reconstructions can significantly enhance the understanding of these phenomena, leading to better decision-making in agriculture through improved irrigation management, in mining through more efficient exploration, and in climate science through more accurate models of ice melt and sea level rise [1–4]. Therefore, developing effective algorithms for reconstructing rough surface profiles is essential, enabling more accurate and actionable insights into these critical remote sensing applications and advancing our ability to monitor and manage the Earth's surface. Much effort has been devoted to this field, for example [5–23]. Common methods include Rytov-type methods [5], Newton-type methods [9–12], reconstruction via sampling (either linear sampling or another type) [13–15], and iterative methods with *ad hoc* guess [20–22]. These traditional methods are generally

based on physical equations of surface scattering, and their robustness is contingent upon certain conditions on surface and incident waves (e.g., the convergence of the iterative method in [21] is based on low-grazing-angle approximation).

Recently, deep learning-type methods have proven to be powerful approaches to dealing with a variety of problems, e.g., image processing, natural language processing, and scientific computing. Studies have been carried out to recover physical scatters from observed field data using a large number of data, e.g., [24–34]. In these works, neural networks are used to learn the mapping from the observed electromagnetic field to the profile of target objects. In particular, in [33,34], a convolutional neural network (CNN)-based deep learning method was developed to reconstruct rough surfaces from the scattered data. It was shown that deep learning methods are capable of solving the inverse scattering problem in a more generalized way. On the other hand, these deep learning methods are highly dependent on 'solution' data (ground truth). In the case of rough surface reconstruction, it is difficult to obtain the entire profile of rough surfaces and corresponding scattered data *a priori*, especially when a large number of data are required. Even if one can create data using simulation, the generated geometric formulations may not be able to adequately capture the features of real-world rough surfaces, resulting in a significant discrepancy in the data's representation, which makes the trained model hard to employ in practice.

Aiming to inherit the efficient learning strategy of data-driven methods while maintaining the physics of rough surface scattering, it is worthwhile to develop a unified method. This motivates us to employ physics-informed neural networks (PINN) [35,36]. PINN is a particular type of deep learning approach developed to solve direct and inverse problems of partial differential equations (PDEs). The main idea of PINN is to employ neural networks as a basis to approximate the 'function' (solution to PDE) and train the neural network by minimizing the 'residual' obtained from the physical information (PDEs), which can be realized using the automatic differentiation. PINN is an unsupervised learning method that does not require any *a priori* knowledge of 'solution' data. PINN has been widely applied to many practical engineering problems; see, for instance, [37–39] for solving the direct problem of electromagnetic scattering, and [40–42] for inverse scattering problems.

In this paper, we develop a novel deep learning method that is based on PINN to reconstruct one-dimensional rough surfaces in two-dimensional media given the information of field data. The physical information (equation) used in the method is the integral representation relating the incident field, the scattered field, and the surface profile. The method of moments (MOM) is used to deal with integral equations; it numerically calculates scattered data from the surface and incident field. A feed-forward neural network serves as a basis to approximate the surface height. The 'predicted' scattered field is then calculated by inserting the predicted surface (in terms of neural network) and its spatial derivatives (obtained by automatic differentiation) into the MOM. The neural network is trained by minimizing the loss between the predicted and observed field data. This renders an unsupervised training scheme that eliminates the need for rough surface data and instead solves the problem using only the field data. The problem is solved using two types of observed field data: full-scattered data and phaseless total field data. In both cases, knowledge of the incident field is required. Both TE and TM fields are considered. We apply the method to recover profiles of Gaussian-correlated random rough surfaces and test the method with a wide range of problem settings including various noise levels, surface scales, surface heights, wavenumbers, and angles of incidence. A large number of numerical results validate the effectiveness and robustness of the proposed approach. The performance of the proposed PINN method is also compared against two conventional techniques: the Newon-type method and the parabolic wave equation method. The source code of implementation is freely available from the GitHub repository [43].

The remainder of this paper is structured as follows. A brief review of integral equations and method of moments is given in Section 2. In Section 3, we introduce a PINN-based deep learning approach to reconstruct one-dimensional rough surfaces from field

data, including the detailed structure of neural networks and loss functions. Numerical experiments are carried out in Section 4, in which the method is tested with a range of problem regimes. Some concluding remarks and potential further directions are drawn in Section 5.

## 2. Background

We consider electromagnetic scattering from a perfectly electrically conducting (PEC) 1D rough surface illuminated by an incident wave, which is depicted in Figure 1.

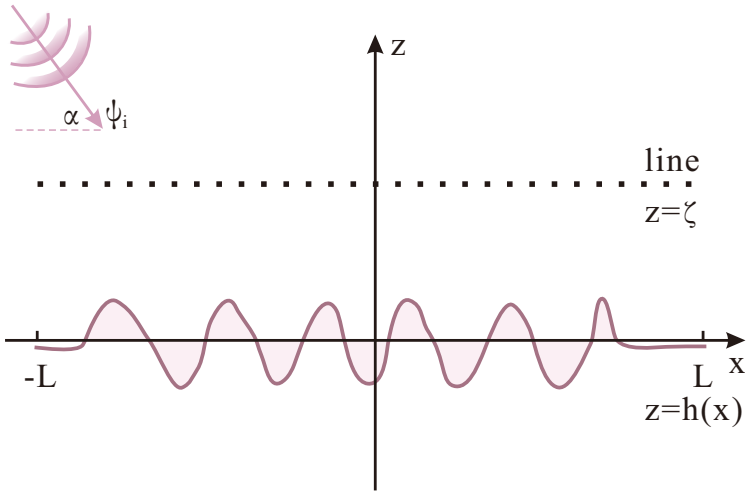


**Figure 1.** Wave scattering from a rough surface illuminated by an incident wave.

The so-called direct problem is to calculate the scattered field given the rough surface shape, whilst the inverse problem is to recover the profile of the rough surface from a set of measured scattered data. It is well known that surface scattering can be formulated by integral equations, which have been widely discussed [44,45]. The method of moments (MOM) is one of the most common numerical techniques to numerically solve integral equations [46,47]. In this section, we provide a brief review of integral equations and the method of moments.

### *2.1. Integral Equations*

Let the coordinate axes be $x$ and $z$, where $x$ is the horizontal and $z$ is the vertical. We consider the time-harmonic scalar wave field $\psi(x,z)$, which is time-independent ($e^{-i\omega t}$ time dependence is discarded). The governing equation for wave scattering is the Helmholtz equation $\nabla^2\psi(x,z)+k^2\psi(x,z)=0$, where $k$ is the wavenumber, defined by $k=2\pi/\lambda$, in which $\lambda$ is the wavelength. Suppose that the 1D PEC rough surface, denoted by $z=h(x)$, is at least second-order differentiable. It has a compact support on $\mathbb{R}$ and perturbs from zero only inside the domain $x\in[-L,L]$. The rough surface is thought of as a rough patch of an extended flat surface on which the integral equation formulation is based here. Let $V$ be the upper homogeneous medium in which the points lie above the surface, i.e., $V=\{(x,z)|z>h(x)\}$, and $S$ is the set of points lying on the surface with $S=\partial V=\{(x,z)|z=h(x)\}$. We write $\mathbf{r},\mathbf{r}'\in V$ as points in the medium and $\mathbf{r_S},\mathbf{r}'_\mathbf{S}\in S$ for the points along the surface. Denote the incident and scattered wave fields as $\psi_i$ and $\psi_s$, respectively, with $\psi=\psi_i+\psi_s$ being the total wave in the space.

The wave field in the upper free space $V$ can be formulated by the Kirchoff–Helmholtz equation [45],

$$\psi(\mathbf{r})=\psi_i(\mathbf{r})+\int_S \mathbf{n}'\cdot\left[\psi(\mathbf{r})\nabla' G(\mathbf{r};\mathbf{r}')-G(\mathbf{r};\mathbf{r}')\nabla'\psi(\mathbf{r}')\right]ds', \tag{1}$$

where $\mathbf{n}'$ is the unit normal vector on the surface, and $G(\mathbf{r};\mathbf{r}')$ is the Green's function to the free space Helmholtz equation given by

$$G(\mathbf{r};\mathbf{r}') = \frac{i}{4}H_0^{(1)}\left(k|\mathbf{r}-\mathbf{r}'|\right), \tag{2}$$

where $H_0^{(1)}$ is the zero-order Hankel function of the first kind. The Kirchoff–Helmholtz equation can be transformed into a pair of coupled integrals by applying boundary conditions. If the Dirichlet boundary condition is assumed, namely, $\psi = 0$ on $S$, which corresponds to the transverse electric (TE) field impinging on a PEC surface, then the coupled integrals become the following:

$$\psi_i(\mathbf{r_S}) = \int_S G(\mathbf{r_S};\mathbf{r'_S})\frac{\partial\psi(\mathbf{r'_S})}{\partial\mathbf{n}'}ds', \tag{3}$$

and

$$\psi_s(\mathbf{r}) = -\int_S G(\mathbf{r};\mathbf{r'_S})\frac{\partial\psi(\mathbf{r'_S})}{\partial\mathbf{n}'}ds', \tag{4}$$

where $\frac{\partial\psi}{\partial\mathbf{n}'} := \mathbf{n}'\cdot\nabla'\psi$, noting that the first equation is obtained via taking the limit as point $\mathbf{r}$ approaches the surface. On the other hand, if we assume the Neumann boundary condition, namely, $\mathbf{n}'\cdot\nabla\psi = 0$ on $S$, which corresponds to the transverse magnetic (TM) field applied on the surface, then the coupled integrals become the following:

$$\psi_i(\mathbf{r_S}) = \frac{1}{2}\psi(\mathbf{r_S}) - \int_S \frac{\partial G(\mathbf{r_S};\mathbf{r'_S})}{\partial\mathbf{n}'}\psi(\mathbf{r'_S})ds', \tag{5}$$

and

$$\psi_s(\mathbf{r}) = \int_S \frac{\partial G(\mathbf{r};\mathbf{r'_S})}{\partial\mathbf{n}'}\psi(\mathbf{r'_S})ds', \tag{6}$$

where $\frac{\partial G}{\partial\mathbf{n}'} := \mathbf{n}'\cdot\nabla'G$, noting that the term $1/2$ in the first equation results from the singularity of the Green's function when limiting the point to the surface.

### *2.2. Method of Moments*

The method of moments (MOM) is used to solve the direct problem, namely, obtain the scattered field from the surface profile. Here, we provide the main matrix equations for the TE and TM fields. A detailed derivation is given in Appendix A. We first discretize the domain $[-L, L]$ uniformly into $N$ subintervals with $(N+1)$ points and denote them as $x_l$ with $l = 0, 1, \ldots, N$, where $x_0 = -L$ and $x_N = L$. The midpoint on each subinverval $[x_{l-1}, x_l]$ is defined as $X_l = 1/2(x_{l-1} + x_l)$ for $l = 1, 2, \ldots, N$. In a typical physical situation, the scattered data in the inverse problem are usually measured along a horizontal line in the medium $V$. We choose to measure the scattered field along the line $z = \zeta$, where $\zeta$ is a constant with $\zeta > h(x),\ x \in [-L, L]$. Denote the discrete points along the surface as $\mathbf{r_n^S} = (X_n, h(X_n))$ and points along the measurement line as $\boldsymbol{q_n} = (X_n, \zeta)$.

Consider first the Dirichlet condition (TE field). We denote $\boldsymbol{\Psi_i}$ and $\boldsymbol{\Psi_s}$ as the vectors of the surface incident field and target scattered field in $\mathbb{C}^N$ with $\boldsymbol{\Psi_i}[l] = \psi_i(X_l, h(X_l))$ and $\boldsymbol{\Psi_s}[l] = \psi_s(X_l, \zeta)$. Then, the discretized form of integral equations for the TE case ((3) and (4)) gives rise to a linear system relating the surface incident field and scattered field as follows:

$$\boldsymbol{\Psi_s} = B_D A_D^{-1}\boldsymbol{\Psi_i}, \tag{7}$$

where $A_D \in \mathbb{C}^{N\times N}$ is given by

$$A_D[n,l] = \int_{x_{l-1}}^{x_l} G(\mathbf{r_n^S};\mathbf{r'_S})\sqrt{1+h'(x')^2}dx', \tag{8}$$

and $B_D \in \mathbb{C}^{N\times N}$ is given by

$$B_D[n,l] = \int_{x_{l-1}}^{x_l} G(\boldsymbol{q_n}; \mathbf{r}'_{\mathbf{S}}) \sqrt{1+h'(x')^2}dx', \tag{9}$$

for $n, l = 1, \ldots, N$. The terms in $A_D$ and $B_D$ are approximated by the trapezium rule.

If the Neumann boundary condition (TM field) is assumed, there is a linear system relating the incident wave and scattered wave from the discretized form of the integral equations for the TM case ((5) and (6)):

$$\boldsymbol{\Psi_s} = B_N A_N^{-1} \boldsymbol{\Psi_i}, \tag{10}$$

where $A_N \in \mathbb{C}^{N\times N}$ is given by

$$A_N[n,l] = \begin{cases} \int_{x_{l-1}}^{x_l} \frac{\partial G(\mathbf{r}^{\mathbf{S}}_{\mathbf{n}}, \mathbf{r}'_{\mathbf{S}})}{\partial \mathbf{n}'} \sqrt{1+h'(x')^2}dx', & n \neq l \\ \frac{1}{2} - \int_{x_{n-1}}^{x_n} \frac{\partial G(\mathbf{r}^{\mathbf{S}}_{\mathbf{n}}, \mathbf{r}'_{\mathbf{S}})}{\partial \mathbf{n}'} \sqrt{1+h'(x')^2}dx', & n = l \end{cases} \tag{11}$$

and $B_N \in \mathbb{C}^{N\times N}$ is given by

$$B_N[n,l] = \int_{x_{l-1}}^{x_l} \frac{\partial G(\boldsymbol{q_n}; \mathbf{r}'_{\mathbf{S}})}{\partial \mathbf{n}'} \sqrt{1+h'(x')^2}dx', \tag{12}$$

for $n, l = 1, \ldots, N$. The terms in $A_N$ and $B_N$ are calculated via the trapezium method.

In general, the scattered field along the line $z = \zeta$ can be written in the operator form of

$$\boldsymbol{\psi_s} = \mathrm{MOM}[h(x), h'(x), h''(x)] := B_h A_h^{-1} \boldsymbol{\psi_i^h}. \tag{13}$$

These operators are all dependent on the surface profile $h$ and its derivatives.

## 3. Reconstruction with a Physics-Informed Neural Network

In this section, a novel unsupervised learning approach is proposed to recover one-dimensional rough surfaces from the field data, which are based on physics-informed neural networks (PINN) [35,36]. The neural network is utilized to approximate the surface height $z = h(x)$ and trained based on the observed field data. The architecture of the proposed learning method is presented in Figure 2. To illustrate the algorithm, we start by introducing some preliminary knowledge (mesh, data, and boundary condition), followed by the neural network structure, the physical information and loss function, and finally, the training scheme.

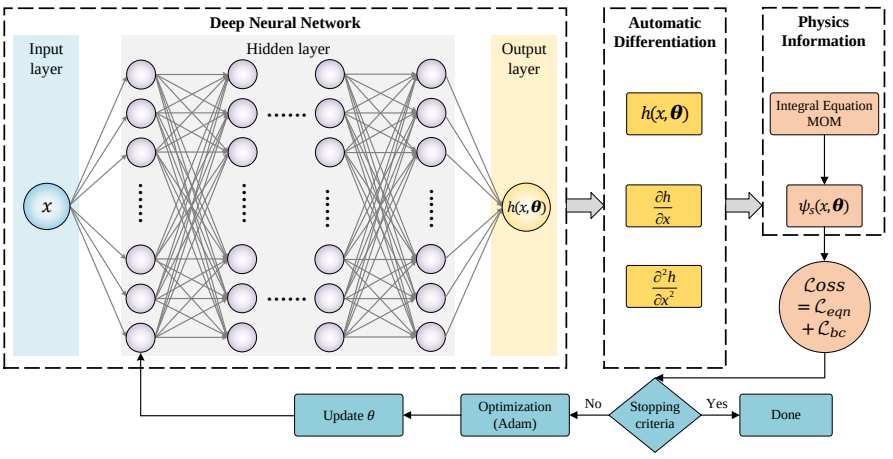


**Figure 2.** An illustrative figure for the PINN-based neural network to reconstruct rough surfaces from field data.

### 3.1. Preliminary

**Sampling Points.** Suppose that we want to recover the rough surface profile on the domain $[-L, L]$. At iteration (epoch) $t$ of training, we first generate a random integer $N_t$ with $N_t \in [N_{\text{obs}}, N_{\text{inv}}]$ where $N_{\text{obs}}$ is the size of observation data, and $N_{\text{inv}}$ is a larger number. The domain $[-L, L]$ is discretized into $(N_t + 1)$ equally spaced points with $x_j^t = j\Delta x_t - L$ for $j = 0, 1, \cdots, N_t$ and $\Delta x_t := 2L/N_t$. The sampling points at the $t$-th iteration of training are the midpoints $X_j^t$ for $j = 1, \ldots, N_t$ with $X_j^t = (x_{j-1}^t + x_j^t)/2$.

**Field Data.** Suppose that field data are collected along a horizontal line $z = \zeta$ at observation points $(X_j^{\text{obs}}, \zeta)$ for $j = 1, 2, \cdots, N_{\text{obs}}$, where $N_{\text{obs}}$ is the number of observation points. Note that the observation points are not aligned with the sampling points. Thus, a set of impulse ('hat-like') piecewise linear functions are employed to interpolate the field data from the observation points $(X_j^{\text{obs}}, \zeta)$ to the collocation points $(X_j^t, \zeta)$. Two types of field data are considered here. In the first case, we assume that full field data can be detected; namely, scattered field $\psi_s^{\text{data}}(X_j^t, \zeta)$ is known. We also consider the case of phaseless field data in which the amplitude of total field $|\psi_{\text{tot}}^{\text{data}}(X_j^t, \zeta)|$ is observed with $|\psi_{\text{tot}}^{\text{data}}| = |\psi_s^{\text{data}} + \psi_i|$. In the numerical examples of Section 4, the field data are numerically generated using the method of moments.

**Boundary Condition.** The method also takes constraints on the boundary values, i.e., surface heights at the edges. We consider that the surface height at close-boundary points $h(X_j^b)$ for $j = 1, 2, \ldots, N_b$ is known, where $X_j^b$ are close-boundary points (they are either close to $L$ or $-L$). In the numerical examples of Section 4, a tapered rough surface is used so that surface height close to the edges decays to zero.

### 3.2. Neural Network

In a standard PINN structure, the solution function (surface profile) is approximated by a neural network, whose inputs and outputs are the same as the surface function, allowing the network to learn the surface function directly. In this research, a fully connected feed-forward deep neural network is employed as basis to approximate the surface function. The neural network is of a uniform structure that has a fixed number of hidden layers and neurons per hidden layer. A nonlinear activation function is applied on the outputs after each hidden layer. The input and output are set to be one-dimensional to predict the function of the surface profile, with the input as one spatial point $x_i$ and the output being the surface height at that point $h(x_i)$. At iteration $t$ of training, we apply the neural network to all the sampling points $X_n^t$ for $n = 1, \ldots, N_t$, leading to the output of surface heights on the entire domain. It is noted that we normalize the input data to the range of $[-1, 1]$, and the output, also conceptualized within the $[-1, 1]$ range, is translated back to the target surface values through inverse normalization. It is noted that normalization of both input and output data has been widely used in deep learning frameworks, since it can significantly accelerate training and improve the stability of neural networks by ensuring consistent scaling across features. In our problem, this normalization (scaling) serves as a form of non-dimensionalization that transforms the errors in field data and surface height at the edges into the range $[-1, 1]$.

### 3.3. Physical Information and Loss Function

At iteration $t$ of training, let $h^{\text{NN}(t)}(x, \boldsymbol{\theta})$ be the predicted surface function in terms of the neural network, where $\boldsymbol{\theta}$ is the set of parameters inside the neural network, including the weights and biases. With the predicted surface height in terms of the neural network, the corresponding spatial derivatives of surface, $\partial h^{\text{NN}(t)}(x, \boldsymbol{\theta})/\partial x$ and $\partial^2 h^{\text{NN}(t)}(x, \boldsymbol{\theta})/\partial x^2$, can be obtained by automatic differentiation. Then, the scattered field along the horizontal line $z = \zeta$ is calculated from the predicted surface and its derivatives via the method of moments (described in Section 2.2). This procedure can be viewed as combining the neural network and physical equations of surface scattering. Denote the calculated scattered field

on the collocation points at $t$-th iteration of training using $\psi_s^{\mathrm{NN}(t)}(X_n^t, \zeta, \boldsymbol{\theta})$, which takes the form of

$$\psi_s^{\mathrm{NN}(t)} = \mathrm{MOM}\left[h^{\mathrm{NN}(t)}, \frac{\partial h^{\mathrm{NN}(t)}}{\partial x}, \frac{\partial^2 h^{\mathrm{NN}(t)}}{\partial x^2}\right]. \tag{14}$$

If full-scattered data are known, the loss function at iteration $t$ is given by a combination of two mean squared errors (MSE), MSE of scattered field ($\mathcal{L}_{\mathrm{eqn}}$), and MSE of boundary values ($\mathcal{L}_{\mathrm{bc}}$):

$$\mathcal{L}(\boldsymbol{\theta}, t) := \underbrace{\frac{1}{N_t}\sum_{j=1}^{N_t}|\psi_s^{\mathrm{NN}(t)}(X_j^t, \zeta, \boldsymbol{\theta}) - \psi_s^{\mathrm{data}}(X_j^t, \zeta)|^2}_{\mathcal{L}_{\mathrm{eqn}}} + \underbrace{\frac{1}{N_b}\sum_{j=1}^{N_b}|h^{\mathrm{NN}(t)}(X_j^b, \boldsymbol{\theta}) - h(X_j^b)|^2}_{\mathcal{L}_{\mathrm{bc}}}. \tag{15}$$

In the case of known phaseless total field data, the loss function at iteration $t$ is composed of MSE of total field data ($\mathcal{L}_{\mathrm{eqn}}$) and MSE of boundary values ($\mathcal{L}_{\mathrm{bc}}$):

$$\mathcal{L}(\boldsymbol{\theta}, t) := \underbrace{\frac{1}{N_t}\sum_{j=1}^{N_t}\left||\psi_{\mathrm{tot}}^{\mathrm{NN}(t)}(X_j^t, \zeta, \boldsymbol{\theta})| - |\psi_{\mathrm{tot}}^{\mathrm{data}}(X_j^t, \zeta)|\right|^2}_{\mathcal{L}_{\mathrm{eqn}}} + \underbrace{\frac{1}{N_b}\sum_{j=1}^{N_b}|h^{\mathrm{NN}(t)}(X_j^b, \boldsymbol{\theta}) - h(X_j^b)|^2}_{\mathcal{L}_{\mathrm{bc}}}, \tag{16}$$

where $\psi_{\mathrm{tot}}^{\mathrm{NN}(t)} = \psi_s^{\mathrm{NN}(t)} + \psi_i$ is the total field obtained by MOM using predicted surface at iteration $t$ of training.

Two remarks can be made here regarding the loss function:

1. The loss function is composed of two parts: the residual of equation $\mathcal{L}_{\mathrm{eqn}}$ and the residual of boundary condition $\mathcal{L}_{\mathrm{bc}}$. Despite their different physical dimensions (the error in field data and in surface values at edges), the normalization process has rendered them dimensionless and scaled both to the range $[-1, 1]$, so no additional non-dimensionalization is required.
2. In our loss function, we assign equal weights to both residual terms. As demonstrated in Section 4, this approach yields highly accurate reconstruction results. Moreover, in inverse scattering theory, the well-posedness of the solution depends on the boundary conditions of the scatterer, specifically, the surface values at the edges of our problem. Therefore, maintaining accurate edge surface values is equally important as minimizing the residual of the governing equation (the error in field data).

### *3.4. Training*

Finally, the loss function is minimized by an optimizer to achieve an 'optimal' set of parameters $\boldsymbol{\theta}$. In this paper, the optimizer is taken to be the Adam (adaptive moment estimation) [48]. During the optimization, a learning rate is used to control how much the weights of the neural network are adjusted with respect to the gradient of the loss function. After training, the neural network serves as an approximate function to the rough surface, where inputting point $x$ yields the output $h(x)$, the predicted surface height at that point. PINN can be viewed as an optimization procedure, via seeking the surface profile, in the neural network space [49], such that minimizes the error in computed and observed field data, and in the surface values at edges.

## 4. Numerical Examples

The performance of the proposed method is tested here. In all numerical examples, the incident field is taken to be a plane wave with $\psi_i(x, z) = \exp(ik(\cos\alpha x + \sin\alpha z))$, where $k$ is the wavenumber and $\alpha$ is the grazing angle (complementary to the angle of incidence). The domain of the rough surface is set as $[-L, L]$ with $L = 8\lambda$, where $\lambda$ is the wavelength

of the incident wave. We apply the method to random Gaussian-correlated rough surfaces, which are generated by an autocorrelation function (a.c.f) given by

$$\rho(\eta) = \langle h(x)h(x+\eta)\rangle = \exp\left(-\frac{\eta^2}{l^2}\right), \tag{17}$$

where $l$ is the surface scale (autocorrelation length). The surface is tapered to zero as $x$ approaches the edges ($x = L$ and $x = -L$) via a tanh function. We focus on the regime in which the roughness is of finite extent on an extended flat surface, which is modeled using a rough surface tapered to zero at the edges; this avoids edge effects sufficiently when using the plane wave as an incident field. All the rough surfaces have a mean zero, and we scale the generated surface vertically to vary the peak-to-trough height ($h_{\max} - h_{\min}$). The field data are measured along the horizontal line $z = \zeta$, and the number of observation points is set to $N_{\text{obs}}$. We consider two cases here:

**Case A**: Full-scattered data are known.
**Case B**: Phaseless total field data (amplitude of field) are known.

If the measured field at one point is $\psi_{\text{data}}$, then the noisy data is given by

$$\psi_{\text{noise}} = \psi_{\text{data}}(1 + \epsilon\delta), \tag{18}$$

where $\epsilon$ is the noise level, and $\delta$ is the random number uniformly generated in $[-1, 1]$. Both the TE field (Dirichlet boundary condition) and TM field (Neumann boundary condition) are considered. We test the method with respect to several characteristics of the rough surface and incident field, including surface scale, peak-to-trough height, wavenumber, and angle of grazing. Throughout Sections 4.1, 4.2, 4.4 and 4.5, the incident field is taken to be the plane wave with wavenumber $k = 2\pi$ (corresponding to frequency of 300MHz and wavelength of 1 meter) and grazing angle $\alpha = -\pi/4$.

As discussed in Section 3, uniform neural networks are employed with $N_l$ hidden layers and $N_n$ neurons per hidden layer, and an activation function is applied after each hidden layer. The structures of neural networks, as well as the optimization parameters, are given in Table 1 for TE and TM fields and case A and case B.

**Table 1.** Structures of neural networks and optimization parameters.

| Field | Case A TE Field | Case B TE Field | Case A TM Field | Case B TM Field |
|---|---|---|---|---|
| $N_l$ | 4 | 6 | 4 | 8 |
| $N_n$ | 256 | 512 | 256 | 512 |
| number of iterations | 1500 | 2000 | 1500 | 2000 |
| activation function | Sigmoid | | | |
| optimizer | Adam | | | |
| learning rate | 0.001 | | | |

The number of sampling points at each iteration is randomly selected from $[N_{\text{obs}}, N_{\text{inv}}]$, where $N_{\text{inv}}$ is a larger number. For the boundary terms in the loss function ($\mathcal{L}_{\text{bc}}$ in (15) and (16)), we take $N_b = 10$ and suppose that $h(X_j^b) = 0$ with $x_j^b = -L + j\Delta x_t$ for $j = 0, 1, \ldots, 4$, and $X_j^b = L - (j-5)\Delta x_t$ for $j = 5, 6, \ldots, 9$.

The quantitative error tested here is the $\ell^2$-norm error between recovered and actual surfaces, given by

$$\|e\|_{\ell^2} = \frac{\|\boldsymbol{H}^{\mathbf{NN}} - \boldsymbol{H}\|_{\ell^2}}{\|\boldsymbol{H}\|_{\ell^2}} \times 100\%, \tag{19}$$

where $\boldsymbol{H}^{\mathbf{NN}}$ is the vector of the reconstructed surface, and $\boldsymbol{H}$ is the vector of the original surface. To analyze the error, we conduct 50 realizations and record both the mean and standard deviation of the $\ell^2$-norm error values.

All the examples are computed using Python. The functionality of neural networks is supported by the open-source library PyTorch [50]. The automatic differentiation is also implemented using PyTorch [51]. The source code of implementation is freely available in the supporting material [43].

### *4.1. Reconstruction with Noiseless Data*

We first test the method using the field data without noise. The surface scale is taken to be $l = 2/3\lambda$, peak-to-trough height is $0.4\lambda$, and the data observation height is $\zeta = 0.5\lambda$. Here, we take $N_{\text{obs}} = 240$, approximately 10 points per surface scale, and $N_{\text{inv}} = 480$, approximately 20 points per surface scale. Figure 3 shows the recovered surface plotted against the true surface for case A (known full-scattered data) and case B (phaseless data) without noise for TE and TM fields.

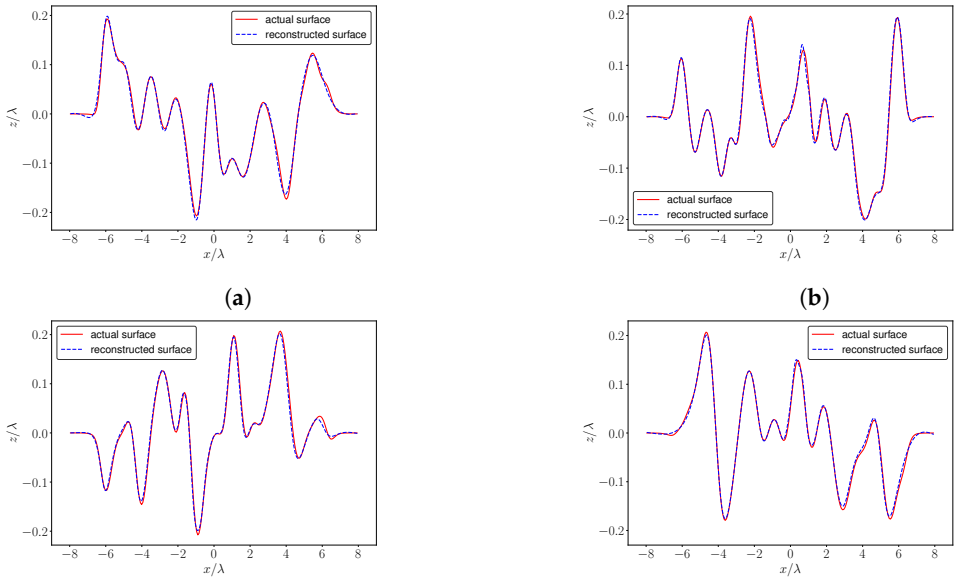


**Figure 3.** Reconstruction of rough surfaces against actual surfaces for case A (known full-scattered data) and case B (known phaseless total field data) using scattered data without noise. (**a**) Case A TE field. (**b**) Case A TM field. (**c**) Case B TE field. (**d**) Case B TM field.

The recovered surface matches the actual surface well by capturing all the shapes. In most parts of the surface, the recovered and actual surfaces closely coincide. The main discrepancy occurs at peaks and troughs of the surface. This is due to the significant change in the derivative of surface, and has also been observed in the results obtained by other traditional methods [6,21].

### *4.2. Reconstruction with Noisy Data*

Here, we add uniformly distributed white noise to the field data and test the results with respect to noise level $\epsilon$. The problem setting is kept the same as in Section 4.1 ($l = 2/3\lambda$, $h_{\max} - h_{\min} = 0.4\lambda$, $\zeta = 0.5\lambda$, $N_{\text{obs}} = 240$, and $N_{\text{inv}} = 480$). The recovered surfaces against the original surfaces with respect to a range of noise levels ($\epsilon$) are shown in Figure 4 for case A (full-scattered field known) and Figure 5 for case B (known phaseless field data). Clearly, with noisy data, the recovered surface still has a close agreement with the actual surface, which validates the robustness of the method in the presence of noise. The discrepancies become more apparent when using data with larger noise levels. Surprisingly, for case A, where full-scattered data are known, this method can tolerate noise with noise levels up

to 20%. It is found that the reconstruction using phaseless data (case B) with small noise level still matches well with the actual surface. As the noise level increases, in particular when $\epsilon > 5\%$, clear discrepancies show up, leading to a much larger error. However, all the 'solution' surfaces in the case B recapture the overall shape of the original ones.

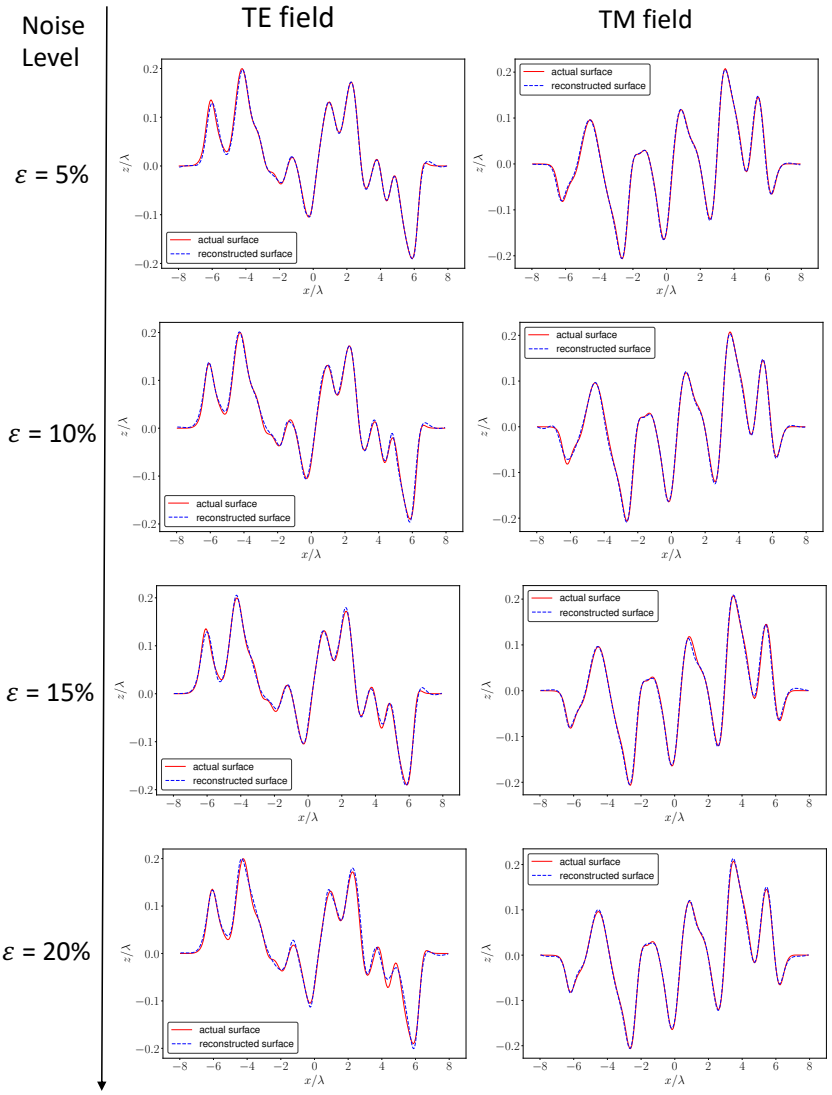


**Figure 4.** Reconstruction of rough surfaces compared to actual surfaces using data with different noise levels $\epsilon$ in case A of known scattered data for TE and TM fields.

We also analyze the error quantitatively. The mean $\ell^2$-norm error, together with the standard deviation with respect to noise level ($\epsilon$), is presented in Figure 6 for case A and case B. For case A with full-scattered data, the error stays at a similar level when noise is small, whereas it rises significantly when the noise level exceeds 15%. This phenomenon is more pronounced in the TE field. In case A, the standard deviation also remains small for small noise levels, but it increases significantly when the noise level is large. In case B with phaseless data, there is a steady increment in the error with noise level for both TE and TM fields. In summary, the method is able to tolerate noise level $\epsilon$ up to around 15% for case A and 5% for case B.

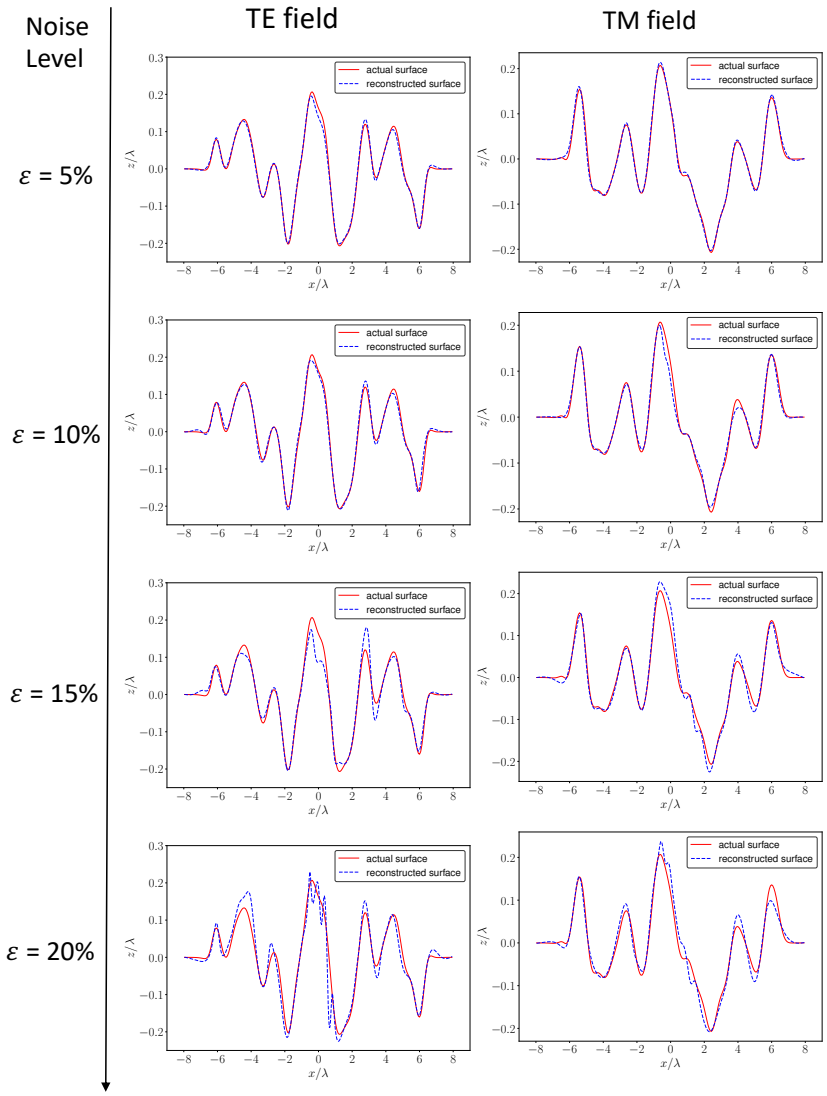


**Figure 5.** Reconstruction of rough surfaces compared to actual surfaces using data with different noise levels $\epsilon$ in case B of known phaseless total field data for TE and TM fields.

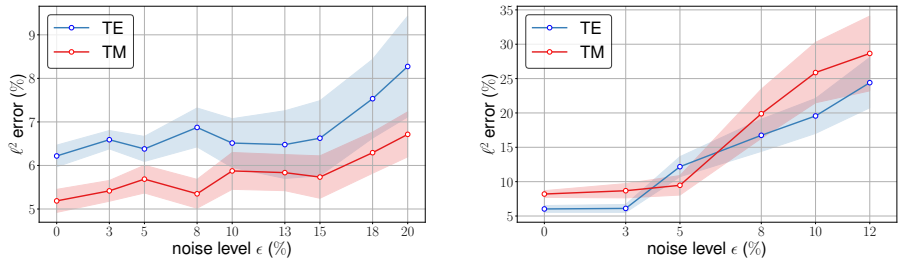


(**a**) (**b**)

**Figure 6.** Mean $\ell^2$-norm error (points) and standard deviation (colored band) with respect to the noise level ($\epsilon$). (**a**) Case A (full-scattered data). (**b**) Case B (phaseless total field data).

### *4.3. Performance Comparison with Conventional Methods*

The performance of the proposed PINN method is compared against conventional techniques here, including the Newton-type method [9] and the parabolic wave equation method [6,21]. The surface parameters remain the same as previously used ($l = 2/3\lambda$, $h_{\max} - h_{\min} = 0.4\lambda$, $\zeta = 0.5\lambda$). We still use $N_{\text{obs}} = 240$ for generating field data, and

$N_{\text{inv}} = 480$ for all three reconstruction algorithms. The results of recovered surfaces using different methods with non-noisy data are shown in Figure 7.

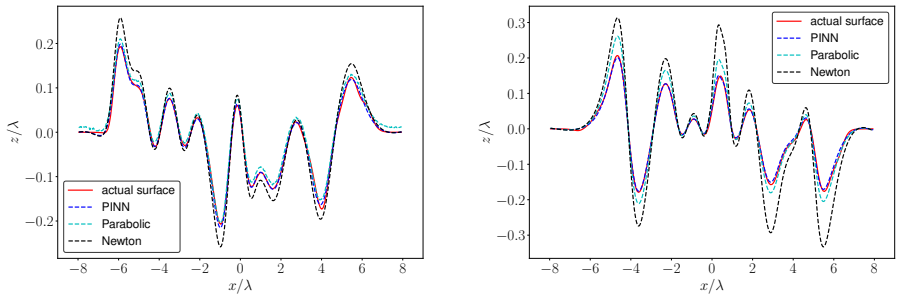


(**a**) (**b**)

**Figure 7.** Comparison of reconstructed surfaces using (i) PINN, (ii) the parabolic wave equation, and (iii) the Newton-type method against the actual surface with non-noisy data. (**a**) Case A TE. (**b**) Case B TM.

As shown, all recovered surfaces from the three methods closely align with the actual surface shape. The parabolic wave equation method performs similarly to the proposed PINN method, whereas the Newton-type method shows reduced effectiveness, particularly in the phaseless scenario. For all three methods, the main discrepancy occurs at peaks and troughs of the surface.

With 5% noisy data, the reconstructed surfaces generated by three methods compared to the original surface are plotted in Figure 8.

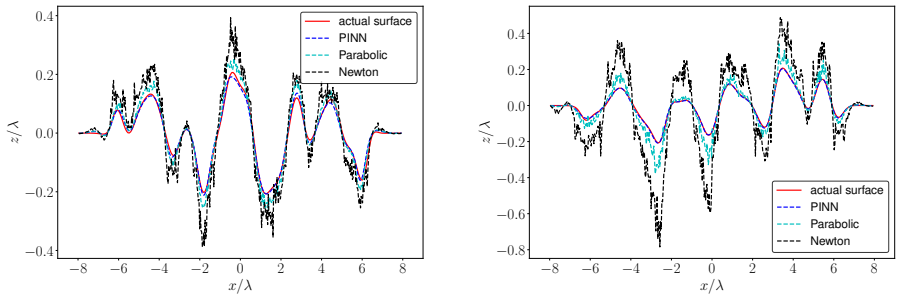


(**a**) (**b**)

**Figure 8.** Comparison of reconstructed surfaces using (i) PINN, (ii) the parabolic wave equation, and (iii) the Newton method against the actual surface with 5% noisy data. (**a**) Case A TE. (**b**) Case B TM.

Reconstructions by conventional methods display certain fluctuations throughout the domain, even though analysis shows that these oscillations are qualitatively similar to the measurement noise. On the other hand, the proposed PINN approach employs a neural network to learn the surface function, which ensures that its result can be much smoother than the conventional method without any oscillation. Therefore, the proposed method has much better performance with noisy field data.

We also list the mean $\ell^2$-norm error between the actual and recovered surfaces generated by (i) the proposed PINN method, (ii) the Newton method, and (iii) the parabolic wave equation method for the TM field in case A (full-scattered data) and the TE field in case B (phaseless total field data) in Table 2. The error is obtained by carrying out 50 realisations for each method and taking the mean value. Clearly, the proposed PINN approach consistently achieves the smallest error in both cases. Notably, conventional methods exhibit significantly higher errors in the presence of noise and may fail entirely when the noise level exceeds 5%, particularly for the Newton method. The primary strength of the proposed method lies in its robustness with respect to noise, maintaining stability even at high noise levels.

Throughout the remainder of the numerical examples, we add 10% noise to the data in case A (full-scattered data) and 3% noise to the data in case B (phaseless total field).

**Table 2.** Mean error in $\ell^2$-norm (%) between the actual and recovered surfaces constructed by three methods.

| Noise Level ($\epsilon$) | Case A TM | | | Case B TE | | |
|---|---|---|---|---|---|---|
| | PINN | Newton | Parabolic | PINN | Newton | Parabolic |
| $\epsilon = 0$ | 5.87 | 7.19 | 6.46 | 8.52 | 10.44 | 9.27 |
| $\epsilon = 3\%$ | 6.14 | 15.84 | 10.74 | 9.38 | 25.74 | 15.29 |
| $\epsilon = 5\%$ | 6.21 | 23.01 | 14.13 | 10.47 | 39.62 | 19.46 |
| $\epsilon = 8\%$ | 6.59 | 29.56 | 18.43 | 15.88 | >50 | 26.91 |
| $\epsilon = 10\%$ | 6.87 | >50 | 23.05 | 18.29 | >50 | 31.66 |

### *4.4. Reconstruction with Respect to Surface Scale*

The surface scale ($l$ in Equation (17)) controls the number of local extrema in the rough surface; smaller $l$ gives rise to more oscillations. We fix $h_{\max} - h_{\min} = 0.4\lambda$ and $\zeta = 0.5\lambda$. The number of observation points is still kept as $N_{\text{inv}} = 240$. As the surface scale decreases, the value of $N_{\text{inv}}$ (maximum number of sampling points at each iteration) has to be increased for two reasons: (i) it becomes more difficult to reconstruct all the finer details for oscillatory surface and (ii) higher resolution helps further reduce the loss during neural network training. Some results of recovered surfaces with respect to relatively small surface scales are shown in Figure 9 for case A and case B, TE and TM fields, and the values of $N_{\text{inv}}$ are also indicated.

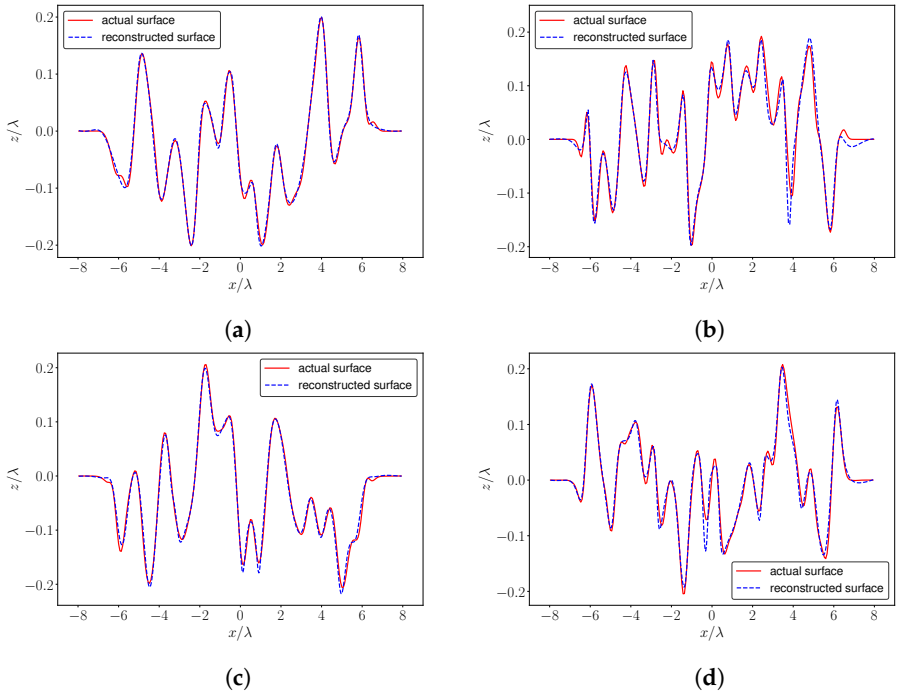


**Figure 9.** Rough surface reconstruction with respect to different values of surface scales ($l$) using full-scattered data (case A) with 10% noise and phaseless total field data (case B) with 3% noise. (**a**) Case A, TE, $l = \frac{1}{2}\lambda$, $N_{\text{inv}} = 600$. (**b**) Case A, TM, $l = \frac{2}{5}\lambda$, $N_{\text{inv}} = 840$. (**c**) Case B, TM, $l = \frac{1}{2}\lambda$, $N_{\text{inv}} = 720$. (**d**) Case B, TE, $l = \frac{2}{5}\lambda$, $N_{\text{inv}} = 840$.

With a larger value of $N_{\text{inv}}$, the recovered surface still captures the overall shape of the original surface. As surface scale decreases, discrepancies become more pronounced, particularly at the peaks and troughs in the highly oscillatory region. Figure 10 presents the mean $\ell^2$-norm error obtained using different values of $N_{\text{inv}}$ with respect to different surface scales ($l$).

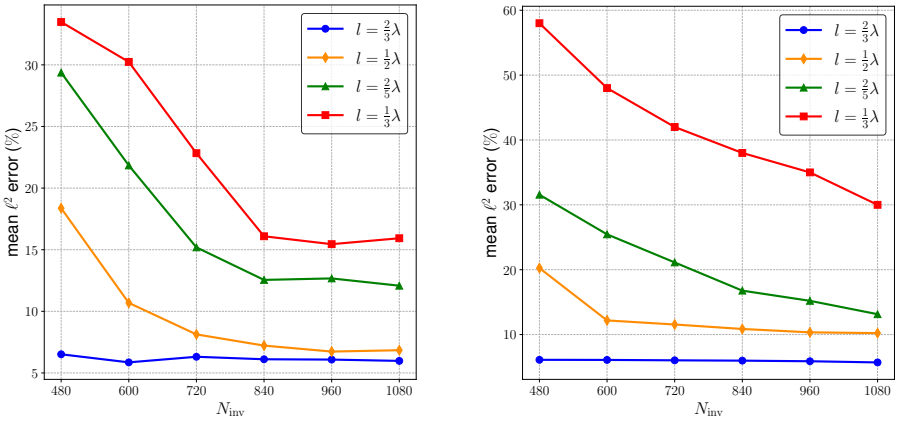


(**a**) (**b**)

**Figure 10.** The mean $\ell^2$-norm error obtained with different values of $N_{\text{inv}}$ (maximum number of testing points at each iteration) and different surface scales $l$. (**a**) Case A TE field. (**b**) Case B TM field.

It is clear that the error decreases with a larger value of $N_{\text{inv}}$. Unsurprisingly, the error is small for a less oscillatory surface (larger value of $l$). The error remains steady provided that $N_{\text{inv}}$ is large enough for $l = 2/3\lambda$ and $l = 1/2\lambda$.

### *4.5. Reconstruction with Respect to Surface Height*

Surface height, in particular the peak-to-trough height ($h_{\max} - h_{\min}$), is a key factor in the inverse problem. Increased height from peak to trough typically leads to stronger surface scattering, resulting in degraded performance of reconstruction algorithms. Here, we solve the problem with parameters of $l = 2/3\lambda$, $\zeta = 2.5h_{\max}$, $N_{\text{obs}} = 240$, and $N_{\text{inv}} = 480$. Some reconstructions of rough surfaces with large peak-to-trough height values for TE and TM fields in case A and case B are shown in Figure 11.

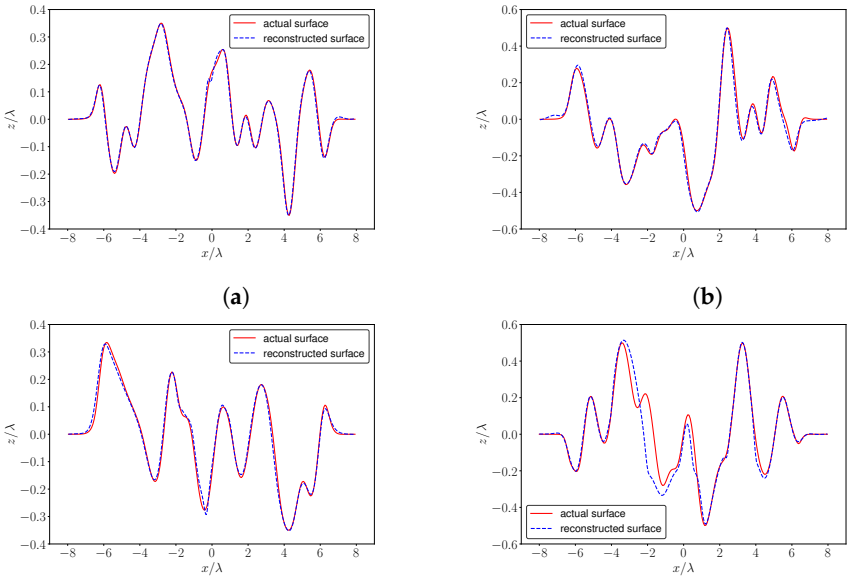


(**a**) (**b**)

(**c**) (**d**)

**Figure 11.** Reconstruction of rough surfaces compared to actual surfaces with respect to different peak-to-trough heights ($h_{\max} - h_{\min}$) for case A (full-scattered data) with 10% noise and case B (phaseless total field data) with 3% noise. (**a**) Case A TM field with $h_{\max} - h_{\min} = 0.7\lambda$. (**b**) Case A TE field with $h_{\max} - h_{\min} = \lambda$. (**c**) Case B TE field with $h_{\max} - h_{\min} = 0.7\lambda$. (**d**) Case B TM field with $h_{\max} - h_{\min} = \lambda$.

The performance degrades for surfaces with larger peak-to-trough height. Overall, despite variations, all the recovered surfaces still manage to preserve the essential features and shapes of the original surfaces. This demonstrates the robustness of the method when dealing with surface height variations.

The mean $\ell^2$-norm error together with the standard deviation with respect to different values of $h_{\max} - h_{\min}$ is presented in Table 3 for case A data with 10% noise and case B data with 3% noise.

**Table 3.** Mean error in $\ell^2$-norm (%) and standard deviation between the actual and recovered surfaces with respect to different peak-to-trough heights.

| $h_{\max} - h_{\min}$ | Case A TE | Case A TM | Case B TE | Case B TM |
|---|---|---|---|---|
| $0.4\lambda$ | $6.57 \pm 0.84$ | $5.87 \pm 0.67$ | $8.52 \pm 1.01$ | $10.72 \pm 2.24$ |
| $0.6\lambda$ | $7.13 \pm 0.95$ | $6.47 \pm 0.83$ | $10.26 \pm 0.96$ | $11.38 \pm 2.87$ |
| $0.8\lambda$ | $7.39 \pm 1.12$ | $8.91 \pm 1.28$ | $11.04 \pm 1.54$ | $11.57 \pm 2.79$ |
| $1.0\lambda$ | $10.55 \pm 2.43$ | $10.36 \pm 2.60$ | $11.37 \pm 2.77$ | $12.45 \pm 3.51$ |
| $1.2\lambda$ | $15.20 \pm 3.11$ | $17.49 \pm 3.52$ | $28.96 \pm 5.84$ | $36.08 \pm 12.39$ |

There is an obvious increase in error for larger surface height, as well as the standard deviation. However, the error is still considerably small when the peak-to-trough height is less than $\lambda$.

### *4.6. Reconstruction with Respect to Incident Wave*

An important aspect of this method is its flexibility with respect to the incident field (wavenumber and angle of incidence). We consider the problem setting of $l = 2/3\lambda$, $h_{\max} - h_{\min} = 0.6\lambda$, $\zeta = 0.6\lambda$, $N_{\text{obs}} = 240$, and $N_{\text{inv}} = 480$, while the wavenumber has been increased to $k = 6.67\pi$ (corresponding to frequency of 1GHz and wavelength of 0.3 m) and the angle of grazing is set to be $-\pi/9$ (corresponding to 10°). The results obtained using the same structure of neural networks (Table 1) for case A TM data with 10% noise and case B TE data with 3% noise are shown in Figure 12.

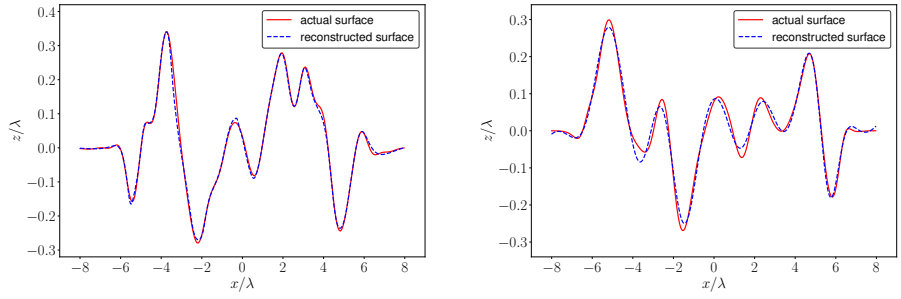


(**a**) (**b**)

**Figure 12.** Reconstruction of rough surfaces compared to actual surfaces from the plane wave of $k = 6.67\pi$ and $\alpha = -10/\pi$ for case A (full-scattered data) with 10% noise and case B (phaseless total field data) with 3% noise. (**a**) Case A TM field. (**b**) Case B TE field.

The reconstructed surface still closely matches the actual surface, which validates the robustness of the method with respect to incident wave characteristics. We make a remark here that the error increases when using incident field with high wavenumber (frequency). However, the error can be reduced via employing deeper neural networks.

## 5. Conclusions

A deep learning approach based on physics-informed neural networks (PINN) has been developed to recover the profile of one-dimensional rough surfaces from observed electromagnetic field data. In this approach, the unknown surface height is approximated by a neural network. The 'physical information' (equations) used in the neural network

are the integral equations relating the surface, incident, and scattered field. With the predicted surface (neural network) and its spatial derivatives (automatic differentiation), we calculate the scattered field via the method of moments (MOM). The neural network is then trained by optimizing the loss between the observed and calculated field data. It was shown that the method can accurately recover highly varying random rough surfaces. The implementation of the proposed method is open-sourced on GitHub, allowing free utilization and further development.

A particular aspect of this approach is that it is an unsupervised reconstruction method; namely, it does not require any '*a priori*' 'solution' data. This is particularly appealing in the rough surface reconstruction field, where it is usually difficult and time-consuming to generate surface data in practice, where a more typical inverse problem is to recover specific unknown surfaces from the measured field data.

Two types of data were considered in this paper: full-scattered field data and phaseless total field data, which results from both TE and TM incident fields. The performance of the method is validated by a large number of test cases with Gaussian-correlated random rough surfaces. The method has also shown strong robustness with respect to a range of different regimes, including noisy data, surface scale (degree of surface oscillations), surface height (peak-to-trough), and incident wave (wavenumber and incidence angle).

Therefore, the proposed method opens up the possibility of treating potential real-world applications of remote sensing through a fast and robust deep-learning approach. This is particularly significant for the recovery and monitoring of glacier and ice sheet dynamics, providing crucial insights into climate change impacts and facilitating more accurate predictions of sea-level rise. Utilizing the proposed PINN-based approach as an unsupervised learning method is especially advantageous because ice sheets and glaciers are constantly changing through time, making it impractical to obtain sufficient labeled data for supervised learning approaches. On the other hand, several challenges may remain when applying the proposed method to real-world monitoring applications:

- In our numerical models, the surface structures are smooth and well-behaved, but in reality, ice sheets and glaciers can exhibit complex, fractal-like geometries or even discontinuities. It is observed that, in our numerical examples, the main discrepancies tend to appear at the peaks and troughs of the surface. If the surface becomes more complex, especially with discontinuities, it becomes increasingly challenging for the method to remain high frequency in these regions. This issue could be resolved by refining the resolution around these problematic areas; however, this approach leads to much longer training time and considerably higher computational cost.
- Our current model considers only two basic wave-scattering cases: transverse electric (TE) and transverse magnetic (TM), while real-world scattering phenomena are far more complex, often involving a mixture of several different types of boundary conditions. In more complex practical scattering scenarios, accurately simulating the direct problem using the integral formulation and method of moments (MoM) becomes challenging, making it difficult to predict the true values of the scattered field data. Since our method relies heavily on the accuracy of these simulations, any discrepancies in the direct problem will significantly affect the reconstruction quality. Even adding a large amount of noise to the data does not fully capture the variability observed in real-world scenarios, making it challenging to achieve good agreement with real data. Therefore, developing a more efficient and accurate model for simulating scattered waves in complex cases is crucial for improving the robustness and effectiveness of the proposed method.

It is noted that even though this paper shows the results of 1D rough surface reconstruction in 2D space, the approach can be easily extended to 3D problems (i.e., recovering 2D rough surfaces). For 3D applications, the main difficulty becomes the time-complexity of the method of moments, which involves a step of inverting a linear system of size $N^2 \times N^2$, where $N$ is the discretization size in one axis. Another important problem to which this method can extend straightforwardly is the design of the inverse waveguide problem. In

the 2D version of the inverse waveguide problem, a pair of rough surfaces need to be reconstructed with respect to a set of field data.

**Author Contributions:** Conceptualization, Y.C., C.W., Y.H., N.V.S., and M.S.; methodology, Y.C., C.W., Y.H., N.V.S., and M.S.; software, Y.C., C.W., Y.H., and N.V.S.; validation, Y.C., C.W., Y.H., N.V.S., and M.S.; formal analysis, Y.C., C.W., Y.H., N.V.S., and M.S.; data curation, Y.C., C.W., Y.H., N.V.S., and M.S.; writing—original draft preparation, Y.C., C.W., Y.H., N.V.S., and M.S.; writing—review and editing, Y.C., C.W., Y.H., N.V.S., and M.S.; supervision, Y.C. and M.S.; funding acquisition, Y.C., C.W., Y.H., and N.V.S. All authors have read and agreed to the published version of the manuscript.

**Funding:** Y.C. was supported by the Youth Program of the Natural Science Foundation of Jiangsu Province (No. BK20230466), the Jiangsu Funding Program for Excellent Postdoctoral Talent (No. 2022ZB584), and Jiangsu Shuangchuang Project (JSSCTD202209). C.W. was supported by the National Natural Science Foundation of China under Grants No. 62301532, in part by the Natural Science Foundation of Jiangsu Province under Grant No. BK20230282. Y.H. acknowledged support from the Qin Chuangyuan cited high-level innovative and entrepreneurial talent project, Shaanxi Province (QCYRCXM-2023-165). N.V.S. acknowledges support from the United Kingdom Research and Innovation-Engineering and Physical Sciences Research Council under "Excalibur-SysGenX: Composable software generation for system-level simulation at exascale", Grant Agreement No. EP/W026635/1.

**Data Availability Statement:** The code of implementation is freely available from the GitHub repository [43].

**Conflicts of Interest:** Author Yuan Hui was employed by the company Shaanxi Logistics Group Co., Ltd. The remaining authors declare that the research was conducted in the absence of any commercial or financial relationships that could be construed as a potential conflict of interest.

## Appendix A. Method of Moments

The appendix gives a brief review of the method of moments, especially how to derive the fundamental linear system from integral equations. Further details on the method of moments for surface scattering can be found in ([52], Chapter 2). The mesh discretization is given in Section 2.2. We consider the Dirichlet condition (TE field) here; the formulations for the Neumann condition (TM field) can be derived in a similar manner. To the leading order, the surface differential on each subinterval $[x_{l-1}, x_l]$ can be treated by a line segment, namely,

$$ds \approx dL = \sqrt{1 + h'(x)^2}dx. \tag{A1}$$

Then, Equation (3) can be written in the following form:

$$\psi_i(\mathbf{r_S}) = \int_0^L G(\mathbf{r_S}; \mathbf{r'_S}) \frac{\partial \psi(x')}{\partial \mathbf{n}'} \sqrt{1 + h'(x')^2}dx'. \tag{A2}$$

Since the wave derivative term $\partial\psi/\partial\mathbf{n}'$ is along the surface, it can be viewed as a function of $x$. Consider the pulse basis function $f_l$ such that

$$f_l(x) = \begin{cases} 1 & \text{if } x \in [x_{l-1}, x_l) \\ 0 & \text{otherwise} \end{cases}, \tag{A3}$$

then the surface derivative can be approximated by

$$\frac{\partial \psi(x')}{\partial \mathbf{n}'} = \sum_{l=1}^{N} J_l f_l(x), \tag{A4}$$

where $J_l$ is defined as the surface derivative at each midpoint, i.e., $J_l = \partial\psi/\partial\mathbf{n}'(X_l, h(X_l))$. Note that in each subinterval $[x_l, x_{l-1})$, $\partial\psi/\partial\mathbf{n}' \approx J_l$; thus, we have

$$\psi_i(\mathbf{r_S}) = \sum_{l=1}^{N} J_l \int_{x_{l-1}}^{x_l} G(\mathbf{r_S}; \mathbf{r'_S}) \sqrt{1 + h'(x')^2} dx'. \tag{A5}$$

Via straightforward point matching, namely set LHS = RHS at all the discrete points $\mathbf{r_n^S} = (X_n, h(X_n))$. Then,

$$\mathbf{\Psi_i}[l] = \sum_{l=1}^{N} J_l \int_{x_{l-1}}^{x_l} G(\mathbf{r_n^S}; \mathbf{r'_S}) \sqrt{1 + h'(x')^2} dx', \tag{A6}$$

which can be expressed as a linear system as follows:

$$\mathbf{\Psi_i} = A_D \boldsymbol{J}, \tag{A7}$$

where $A_D \in \mathbb{C}^{N\times N}$ is given in Equation (8). Similarly, we apply the pulse basis function and Equation (A4) to the scattered field integral Equation (4); then, the scattered field along the measurement line can be written in the following form:

$$\psi_s(\boldsymbol{q}) = -\sum_{l=1}^{N} J_l \int_{x_{l-1}}^{x_l} G(\boldsymbol{q}; \mathbf{r'_S}) \sqrt{1 + h'(x')^2} dx', \tag{A8}$$

where $\boldsymbol{q} = (x, \zeta)$. Again, using point matching with respect to all the discrete points $\boldsymbol{q_n} = (X_n, \zeta)$, we get

$$\psi_s(\boldsymbol{q_n}) = -\sum_{l=1}^{N} J_l \int_{x_{l-1}}^{x_l} G(\boldsymbol{q_n}; \mathbf{r'_S}) \sqrt{1 + h'(x')^2} dx', \tag{A9}$$

which leads to the linear system

$$\mathbf{\Psi_s} = B_D \boldsymbol{J}. \tag{A10}$$

Combining Equation (A7) and Equation (A10), we obtain Equation (7), the fundamental linear system for the TE field.

## References


1. Schmugge, T. Remote Sensing of Surface Soil Moisture. *J. Appl. Meteorol. (1962–1982)* **1978**, *17*, 1549–1557. [CrossRef]
2. Massonnet, D.; Feigl, K.L. Radar interferometry and its application to changes in the Earth's surface. *Rev. Geophys.* **1998**, *36*, 441–500. [CrossRef]
3. Engman, E.T. Applications of microwave remote sensing of soil moisture for water resources and agriculture. *Remote Sens. Environ.* **1991**, *35*, 213–226. [CrossRef]
4. Baumhoer, C.A.; Dietz, A.J.; Dech, S.; Kuenzer, C. Remote Sensing of Antarctic Glacier and Ice-Shelf Front Dynamics—A Review. *Remote Sens.* **2018**, *10*, 1445. [CrossRef]
5. Schatzberg, A.; Devaney, A.J. Rough surface inverse scattering within the Rytov approximation. *J. Opt. Soc. Am. A* **1993**, *10*, 942–950. [CrossRef]
6. Chen, Y.; Spivack, M. Rough surface reconstruction at grazing angles by an iterated marching method. *J. Opt. Soc. Am. A* **2018**, *35*, 504–513. [CrossRef]
7. Chen, Y.; Rath Spivack, O.; Spivack, M. Recovery of rough surface in ducting medium from grazing angle scattered wave. *J. Appl. Phys.* **2018**, *124*, 084901. [CrossRef]
8. Akduman, I.; Kress, R.; Yapar, A. Iterative reconstruction of dielectric rough surface profiles at fixed frequency. *Inverse Probl.* **2006**, *22*, 939. [CrossRef]
9. Kress, R.; Tran, T. Inverse scattering for a locally perturbed half-plane. *Inverse Probl.* **2000**, *16*, 1541. [CrossRef]
10. Yapar, A.; Ozdemir, O.; Sahinturk, H.; Akduman, I. A Newton method for the reconstruction of perfectly conducting slightly rough surface profiles. *IEEE Trans. Antennas Propag.* **2006**, *54*, 275–279. [CrossRef]
11. Mojabi, P.; LoVetri, J. Overview and Classification of Some Regularization Techniques for the Gauss-Newton Inversion Method Applied to Inverse Scattering Problems. *IEEE Trans. Antennas Propag.* **2009**, *57*, 2658–2665. [CrossRef]

12. Bozza, G.; Pastorino, M. An Inexact Newton-Based Approach to Microwave Imaging Within the Contrast Source Formulation. *IEEE Trans. Antennas Propag.* **2009**, *57*, 1122–1132. [CrossRef]
13. Li, J.; Yang, J.; Zhang, B. A linear sampling method for inverse acoustic scattering by a locally rough interface. *Inverse Probl. Imaging* **2021**, *15*, 1247–1267. [CrossRef]
14. Xu, X.; Zhang, B.; Zhang, H. Uniqueness and Direct Imaging Method for Inverse Scattering by Locally Rough Surfaces with Phaseless Near-Field Data. *SIAM J. Imaging Sci.* **2019**, *12*, 119–152. [CrossRef]
15. Ji, X.; Liu, X.; Zhang, B. Inverse Acoustic Scattering with Phaseless Far Field Data: Uniqueness, Phase Retrieval, and Direct Sampling Methods. *SIAM J. Imaging Sci.* **2019**, *12*, 1163–1189. [CrossRef]
16. Dolcetti, G.; Alkmim, M.; Cuenca, J.; De Ryck, L.; Krynkin, A. Robust reconstruction of scattering surfaces using a linear microphone array. *J. Sound Vib.* **2021**, *494*, 115902. [CrossRef]
17. Sefer, A. Locally Perturbed Inaccessible Rough Surface Profile Reconstruction via Phaseless Scattered Field Data. *IEEE Trans. Geosci. Remote Sens.* **2022**, *60*, 2002808. [CrossRef]
18. Sefer, A.; Yapar, A. Inverse Scattering by Perfectly Electric Conducting (PEC) Rough Surfaces: An Equivalent Model With Line Sources. *IEEE Trans. Geosci. Remote Sens.* **2022**, *60*, 2007109. [CrossRef]
19. Sefer, A.; Yapar, A.; Yelkenci, T. Imaging of Rough Surfaces by RTM Method. *IEEE Trans. Geosci. Remote Sens.* **2024**, *62*, 2003312. [CrossRef]
20. Sefer, A.; Yapar, A. An Iterative Algorithm for Imaging of Rough Surfaces Separating Two Dielectric Media. *IEEE Trans. Geosci. Remote Sens.* **2021**, *59*, 1041–1051. [CrossRef]
21. Chen, Y.; Spivack, O.R.; Spivack, M. Rough surface reconstruction from phaseless single frequency data at grazing angles. *Inverse Probl.* **2018**, *34*, 124002. [CrossRef]
22. Qu, F.; Zhang, B.; Zhang, H. A Novel Integral Equation for Scattering by Locally Rough Surfaces and Application to the Inverse Problem: The Neumann Case. *SIAM J. Sci. Comput.* **2019**, *41*, A3673–A3702. [CrossRef]
23. Wombell, R.J.; DeSanto, J.A. Reconstruction of rough-surface profiles with the Kirchhoff approximation. *J. Opt. Soc. Am. A* **1991**, *8*, 1892–1897. [CrossRef]
24. Zhou, Y.; Zhong, Y.; Wei, Z.; Yin, T.; Chen, X. An Improved Deep Learning Scheme for Solving 2-D and 3-D Inverse Scattering Problems. *IEEE Trans. Antennas Propag.* **2020**, *69*, 2853–2863. [CrossRef]
25. Xu, K.; Wu, L.; Ye, X.; Chen, X. Deep Learning-Based Inversion Methods for Solving Inverse Scattering Problems With Phaseless Data. *IEEE Trans. Antennas Propag.* **2020**, *68*, 7457–7470. [CrossRef]
26. Xu, K.; Zhang, C.; Ye, X.; Song, R. Fast Full-Wave Electromagnetic Inverse Scattering Based on Scalable Cascaded Convolutional Neural Networks. *IEEE Trans. Geosci. Remote Sens.* **2022**, *60*, 2001611. [CrossRef]
27. Guo, R.; Song, X.; Li, M.; Yang, F.; Xu, S.; Abubakar, A. Supervised Descent Learning Technique for 2-D Microwave Imaging. *IEEE Trans. Antennas Propag.* **2019**, *67*, 3550–3554. [CrossRef]
28. Sabbaghi, M.; Zhang, J.; Hanson, G.W. Machine Learning Target Count Prediction in Electromagnetics Using Neural Networks. *IEEE Trans. Antennas Propag.* **2022**, *70*, 6171–6183. [CrossRef]
29. Sanghvi, Y.; Kalepu, Y.; Khankhoje, U.K. Embedding Deep Learning in Inverse Scattering Problems. *IEEE Trans. Comput. Imaging* **2020**, *6*, 46–56. [CrossRef]
30. Chen, G.; Shah, P.; Stang, J.; Moghaddam, M. Learning-Assisted Multimodality Dielectric Imaging. *IEEE Trans. Antennas Propag.* **2020**, *68*, 2356–2369. [CrossRef]
31. Li, L.; Wang, L.G.; Teixeira, F.L.; Liu, C.; Nehorai, A.; Cui, T.J. DeepNIS: Deep Neural Network for Nonlinear Electromagnetic Inverse Scattering. *IEEE Trans. Antennas Propag.* **2019**, *67*, 1819–1825. [CrossRef]
32. Zong, Z.; Wang, Y.; Wei, Z. A Wavelet-Based Compressive Deep Learning Scheme for Inverse Scattering Problems. *IEEE Trans. Geosci. Remote Sens.* **2022**, *60*, 2007511. [CrossRef]
33. Aydin, I.; Budak, G.; Sefer, A.; Yapar, A. CNN-Based Deep Learning Architecture for Electromagnetic Imaging of Rough Surface Profiles. *IEEE Trans. Antennas Propag.* **2022**, *70*, 9752–9763. [CrossRef]
34. Izde Aydin, Guven Budak, A.S.; Yapar, A. Recovery of impenetrable rough surface profiles via CNN-based deep learning architecture. *Int. J. Remote Sens.* **2022**, *43*, 5658–5685. [CrossRef]
35. Raissi, M.; Perdikaris, P.; Karniadakis, G. Physics–informed neural networks: A deep learning framework for solving forward and inverse problems involving nonlinear partial differential equations. *J. Comput. Phys.* **2019**, *378*, 686–707. [CrossRef]
36. Karniadakis, G.E.; Kevrekidis, I.G.; Lu, L.; Perdikaris, P.; Wang, S.; Yang, L. Physics–informed machine learning. *Nat. Rev. Phys.* **2021**, *3*, 422–440. [CrossRef]
37. Rasht-Behesht, M.; Huber, C.; Shukla, K.; Karniadakis, G.E. Physics-Informed Neural Networks (PINNs) for Wave Propagation and Full Waveform Inversions. *J. Geophys. Res. Solid Earth* **2022**, *127*, e2021JB023120. [CrossRef]
38. Alkhadhr, S.; Liu, X.; Almekkawy, M. Modeling of the Forward Wave Propagation Using Physics-Informed Neural Networks. In Proceedings of the 2021 IEEE International Ultrasonics Symposium (IUS), Xi'an, China, 11–16 September 2021; pp. 1–4. [CrossRef]
39. Yin, Z.; Li, G.Y.; Zhang, Z.; Zheng, Y.; Cao, Y. SWENet: A physics-informed deep neural network (PINN) for shear wave elastography. *IEEE Trans. Med. Imaging* **2024**, *43*, 1434–1448. [CrossRef]
40. Chen, Y.; Lu, L.; Karniadakis, G.E.; Negro, L.D. Physics–informed neural networks for inverse problems in nano-optics and metamaterials. *Opt. Express* **2020**, *28*, 11618–11633. [CrossRef]

41. Guo, R.; Lin, Z.; Shan, T.; Song, X.; Li, M.; Yang, F.; Xu, S.; Abubakar, A. Physics Embedded Deep Neural Network for Solving Full-Wave Inverse Scattering Problems. *IEEE Trans. Antennas Propag.* **2022**, *70*, 6148–6159. [CrossRef]
42. Hu, Y.D.; Wang, X.H.; Zhou, H.; Wang, L.; Wang, B.Z. A More General Electromagnetic Inverse Scattering Method Based on Physics-Informed Neural Network. *IEEE Trans. Geosci. Remote Sens.* **2023**, *61*, 4505109. [CrossRef]
43. Chen, Y. Supporting Material. 2024. Available online: https://github.com/yc397/pinn_rough_surface (accessed on 1 May 2024).
44. Warnick, K.F.; Chew, W.C. Numerical simulation methods for rough surface scattering. *Waves Random Media* **2001**, *11*, R1. [CrossRef]
45. Voronovich, A.G. *Wave Scattering from Rough Surfaces*; Springer Science & Business Media: Berlin/Heidelberg, Germany, 2013; Volume 17.
46. Harrington, R.F. *Field Computation by Moment Methods*; Wiley-IEEE Press: Hoboken, NJ, USA, 1993.
47. Bourlier, C.; Pinel, N.; Kubické, G. *Method of Moments for 2D Scattering Problems: Basic Concepts and Applications*; John Wiley & Sons: Hoboken, NJ, USA, 2013.
48. Kingma, D.P.; Ba, J. Adam: A method for stochastic optimization. *arXiv* **2014**, arXiv:1412.6980.
49. Cybenko, G. Approximation by superpositions of a sigmoidal function. *Math. Control Signals Syst.* **1989**, *2*, 303–314. [CrossRef]
50. Paszke, A.; Gross, S.; Massa, F.; Lerer, A.; Bradbury, J.; Chanan, G.; Killeen, T.; Lin, Z.; Gimelshein, N.; Antiga, L.; et al. PyTorch: An imperative style, high-performance deep learning library. In Proceedings of the 33rd International Conference on Neural Information Processing Systems, Vancouver, BC, Canada, 8–14 December 2019; Curran Associates Inc.: Red Hook, NY, USA, 2019.
51. Paszke, A.; Gross, S.; Chintala, S.; Chanan, G.; Yang, E.; DeVito, Z.; Lin, Z.; Desmaison, A.; Antiga, L.; Lerer, A. Automatic Differentiation in PyTorch. In Proceedings of the NeurIPS Autodiff Workshop, Long Beach, CA, USA, 9 December 2017.
52. Tsang, L.; Kong, J.A.; Ding, K.H.; Ao, C.O. *Scattering of Electromagnetic Waves: Numerical Simulations*; John Wiley & Sons: Hoboken, NJ, USA, 2001. [CrossRef]